Chapter 4
Void Growth to Coalescence: Unit Cell and Analytical Modelling

4.1 Void Shape Evolution During Ductile Fracture

The voids in a ductile material subjected to plastic deformation change shape according to the local plastic flow of the material since the voids are not internally pressurized. As a result, the void growth rate and shape evolution are intrinsically linked because the void shape (and orientation) induce anisotropy, altering the stress state and the growth rate in a non-linear fashion. The standard Gurson-Tvergaard model maintains its isotropic formulation by enforcing the void to remain spherical. The influence of the void shape on the stress response of the material is shown in Fig. 4.1 as well as the variation in the growth rate in Fig. 4.2 for a practical stress triaxiality of 2/3 (equal-biaxial stretching).

To simplify the modelling procedure, it is often assumed that the voids can be approximated as spheroids (an ellipsoid of revolution) as shown in Fig. 4.3. In uniaxial tension, void shape evolution is significant as initially penny-shaped voids can rapidly elongate in the principal loading direction into prolate voids. Alternatively, at high stress triaxialities found ahead of a crack tip, the voids tend to grow laterally and become oblate regardless of the principal loading direction. Penny-shaped voids are the exception to this trend and only appreciably grow in the opening direction even at high stress triaxiality (Lassance et al. 2006; Butcher 2011). Furthermore, a specific stress triaxiality exists for each void shape that will enforce the void to grow in a self-similar manner and retain its shape. Consequently, the mechanics for modeling void shape evolution are complex and no analytical model has yet been developed that can account for the void shape evolution in different stress states. As such, the adoption of heuristic parameters in these models is currently unavoidable (Keralavarma and Benzerga 2010).

The evolution of the void shape is a function of the initial void size, f_i, initial aspect ratio, W_i, equivalent plastic strain, $\bar{\varepsilon}^p$, matrix hardening exponent, n, and stress state, σ_{ij}, in the general form

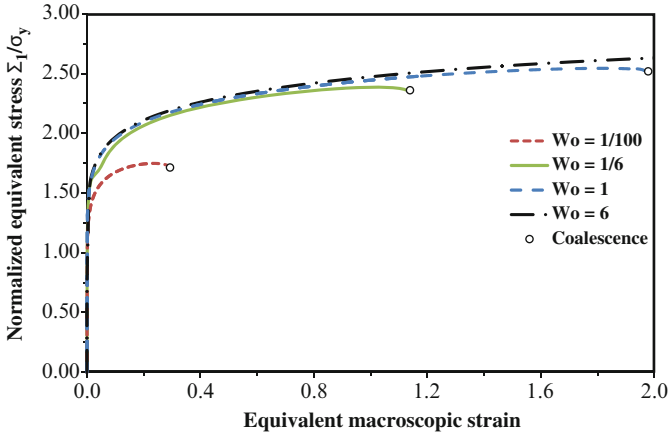$$W = g(f_i, W_i, T, n, \bar{\varepsilon}^p) \tag{4.1}$$

Fig. 4.1 Normalized equivalent stress response of an axisymmetric voided unit cell with various void shapes
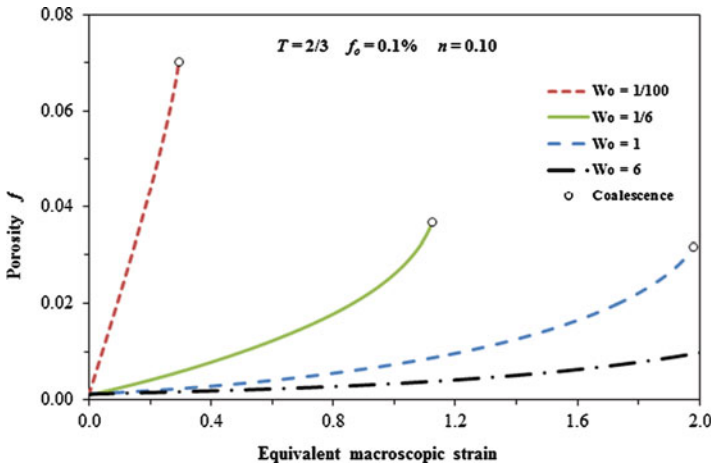

Fig. 4.2 Variation of void growth in an axisymmetric unit cell with the initial void shape. The assumption of a constant spherical void in the standard GT model significantly overestimates void growth for prolate voids and underestimate growth for oblate voids in the practical triaxiality regime (T < 1)

4.2   Damage-Based Material Models with Void Shape Effects

The physical foundation of a damage-based constitutive model rests upon the accuracy of the analytical sub-models that describe void nucleation, evolution, coalescence and material softening. While numerous micromechanical models have been proposed in the literature that can capture damage evolution, at least qualitatively, the veracity of these models must be evaluated over the large number of void shapes, sizes and stress states that will be found within a real microstructure.
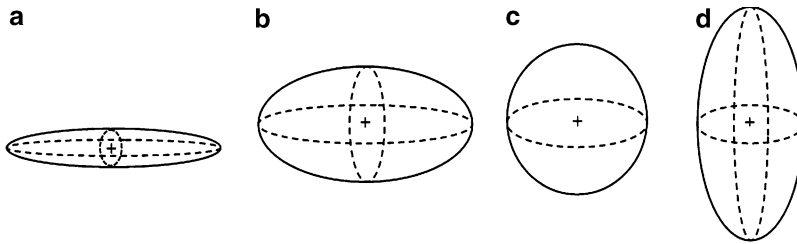
Fig. 4.3 Idealized spheroidal void shapes. (**a**) Penny-shaped spheroid: $W \rightarrow 0$, (**b**) oblate spheroid: $W < 1$, (**c**) sphere: $W = 1$, (**d**) prolate spheroid: $W > 1$

Finite-element simulations of axisymmetric unit cells containing different void geometries are required to provide the numerical benchmarks for these evolution models. An emphasis will be placed upon the evolution of penny-shaped voids because they are nucleated by particle cracking and have received scant attention in the literature. The organization of the section is as follows:

- Finite-element modeling and analysis of voided unit cells
- Discussion of finite-element simulations for a range of void aspect ratios and initial porosities
- Evaluation of current micromechanical models to predict damage evolution
- Development of unit cell correlations for damage evolution

4.3   Modeling Void Evolution Using a Unit Cell

The voids within a bulk material are assumed to be distributed throughout the material in such a manner that the material may be considered to be composed of identical unit cells, each containing a single void at its center. Typically, the unit cells are assumed to be cubic or axisymmetric. The axisymmetric unit cell is obtained by assuming the material is composed of interlocking hexagonal unit cells. These hexagonal unit cells can be approximated as cylindrical and then reduced to one-quarter, 2-D axisymmetric geometry for finite-element modelling as shown in Fig. 4.4. Similarly, the geometry of a 3-D cubic unit cell can be directly reduced to a one-eighth model due to symmetry.

The predicted trends for damage evolution are somewhat dependent upon the type of unit cell geometry (Kuna and Sun 1996). The evolution of porosity is lowest in a 3-D model and highest in the axisymmetric model due to the 3-D material containing more material to constrain the growth of the void and delay coalescence. As seen in Fig. 4.5, the cubic unit cell requires a significantly larger number of elements than the axisymmetric model and requires 8-node solid brick elements that are significantly more computationally expensive than the 4-node quadrilaterals used in the axisymmetric model. As a result, the run-times for cubic cells tend to be prohibitive unless a specific loading condition or geometry mandates their use. In the literature, most unit
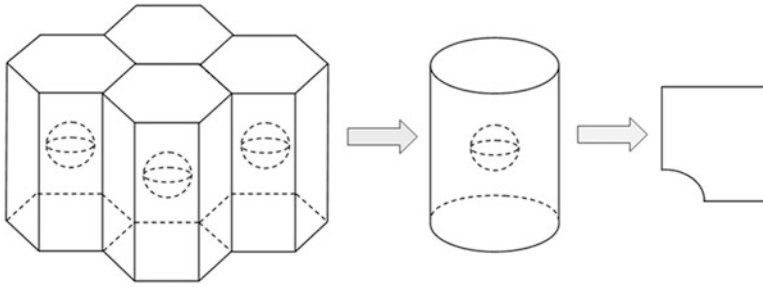
Fig. 4.4 Procedure for approximating a hexagonal distribution of unit cells into an axisymmetric cell model that can be reduced to a one-quarter, 2-D geometry for finite-element modeling
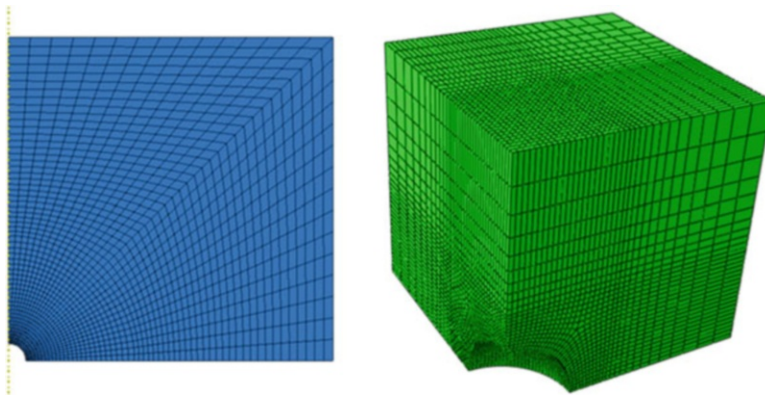

Fig. 4.5 Typical cell geometry and finite-element mesh for an initially spherical void in a one-quarter axisymmetric unit cell (*left*) and a one-eight cubic unit cell (*right*)

cell studies have focused on the use of axisymmetric geometries as they are efficient and provide a good estimate for damage evolution and fracture strains (Koplik and Needleman 1988; Kuna and Sun 1996; Brocks et al. 1996; Pardoen and Hutchinson 2000). It should be emphasized that axisymmetric models provide a lower, and therefore, more conservative estimate for the fracture strain (coalescence) than their 3-D counterparts. Axisymmetric unit cells are considered in the present work to generate the void evolution trends required for validation of the micromechanical models.

4.3.1   Analysis of an Axisymmetric Unit Cell

The axisymmetric unit cell is analyzed using a cylindrical coordinate system denoted by (e_r, e_θ, e_z) along the r-radial, θ-ortho-radial and z-axial axes, respectively. As shown in Fig. 4.6, the geometry of the cylindrical unit cell is defined by a height
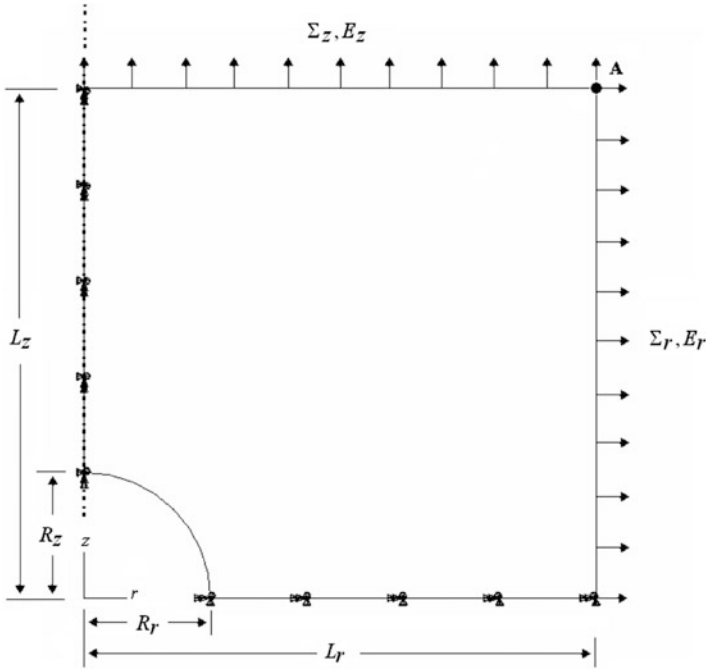
Fig. 4.6 General geometry and boundary conditions used to model the one-quarter axisymmetric unit cell

of $2L_z$ and radius, L_r and contains a spheroidal void with radii, R_z and R_r. The void shape is a prolate spheroid when $R_z > R_r$, an oblate spheroid when $R_z < R_r$, or a sphere when $R_z = R_r$. The geometry of the unit cell and void are defined using non-dimensional parameters. The void is defined by its volume fraction or porosity, f, and its aspect ratio, W, while the cell geometry is defined by its aspect ratio, λ. These parameters can also be combined to calculate the void spacing ratio (ligament size ratio), χ, that plays a critical role in void coalescence. These parameters all evolve during deformation of the cell and their initial values are defined as

$$f_0 = \frac{2R_{z0}}{3L_{z0}}\left(\frac{R_{r0}}{L_{r0}}\right)^2 \quad W_0 = \frac{R_{z0}}{R_{r0}} \quad \lambda_0 = \frac{L_{z0}}{L_{r0}}$$

$$\chi_0 = \frac{R_{r0}}{L_{r0}} = \left(\frac{3}{2}f_0\frac{\lambda_0}{W_0}\right)^{1/3} \qquad (4.2\text{--}4.5)$$

A number of important and useful relations can be obtained to describe the microstructure of a voided unit cell and its evolution. First, consider a general voided unit cell subjected to an arbitrary deformation process. The unit cell has the half-lengths L_1, L_2, L_3 that are coincident with the principal loading directions. The unit cell contains an arbitrarily oriented ellipsoidal void with semi-axes denoted as R_1, R_2 and R_3. The porosity (void volume fraction) of the cell is defined as

$$\frac{V_{\text{void}}}{V_{\text{cell}}} = \frac{f}{\gamma_{\text{cell}}} = \frac{R_1 R_2 R_3}{L_1 L_2 L_3} = \frac{W_1}{\lambda_1}\frac{W_2}{\lambda_2}\chi_2^3\chi = \chi_1\chi_2\chi_3 \tag{4.6}$$

where W_i are the void aspect ratios; λ_i are the cell aspect ratios; χ_i are the void spacing (or ligament size) ratios and γ_{cell} is a shape parameter specific to the assumed unit cell with $\gamma = 2/3$ for an axisymmetric unit cell and $\gamma = \pi/6$ for a cubic cell.

The void aspect ratios, spacing ratios, and cell aspect ratios can be defined as

$$W_1 = \frac{R_1}{R_2} \quad W_2 = \frac{R_3}{R_2} \quad \chi_i = \frac{R_i}{L_i} \quad \lambda_1 = \frac{L_1}{L_2} \quad \lambda_2 = \frac{L_3}{L_2} \tag{4.7–4.11}$$

Taking the derivative of Eqs. (4.6–4.11) with respect to time, it is straightforward to obtain the following relations as a function of the macroscopic principal strain rates as

$$\frac{\dot{f}}{f} = \frac{\dot{R}_1}{R_1} + \frac{\dot{R}_2}{R_2} + \frac{\dot{R}_3}{R_3} - \dot{E}_1 - \dot{E}_2 - \dot{E}_3 \tag{4.12–4.17}$$

$$\frac{\dot{W}_1}{W_1} = \frac{\dot{R}_1}{R_1} - \frac{\dot{R}_2}{R_2} \quad \frac{\dot{W}_2}{W_2} = \frac{\dot{R}_3}{R_3} - \frac{\dot{R}_2}{R_2} \quad \frac{\dot{\chi}_i}{\chi_i} = \frac{\dot{R}_i}{R_i} - \dot{E}_i \quad \frac{\dot{\lambda}_1}{\lambda_1} = \dot{E}_1 - \dot{E}_2 \quad \frac{\dot{\lambda}_2}{\lambda_2} = \dot{E}_3 - \dot{E}_2$$

From Eqs. (4.12–4.17), the growth rates of the void semi-axes can be expressed as

$$\frac{\dot{R}_1}{R_1} = \dot{E}_{\text{hyd}} + \frac{1}{3}\left(\frac{\dot{f}}{f} + 2\frac{\dot{W}_1}{W_1} - \frac{\dot{W}_2}{W_2}\right) \tag{4.18}$$

$$\frac{\dot{R}_2}{R_2} = \dot{E}_{\text{hyd}} + \frac{1}{3}\left(\frac{\dot{f}}{f} - \frac{\dot{W}_1}{W_1} - \frac{\dot{W}_2}{W_2}\right) \tag{4.19}$$

$$\frac{\dot{R}_3}{R_3} = \dot{E}_{\text{hyd}} + \frac{1}{3}\left(\frac{\dot{f}}{f} - \frac{\dot{W}_1}{W_1} + 2\frac{\dot{W}_2}{W_2}\right) \tag{4.20}$$

Alternatively, using only the void spacing ratios, the evolution rate of the porosity can be expressed as

$$\frac{\dot{f}}{f} = \frac{\dot{\chi}_1}{\chi_1} + \frac{\dot{\chi}_2}{\chi_2} + \frac{\dot{\chi}_3}{\chi_3} \tag{4.21}$$

The above Eqs. (4.6–4.21) are valid for any type of unit cell or ellipsoidal void geometry and reduce accordingly depending on the type of geometry considered. For example, an axisymmetric unit cell with the void semi-axes coincident with the principal loading directions: $\dot{W}_2/W_2 = 0$, $\dot{\lambda}_2/\lambda_2 = 0$ and $\dot{\chi}_2/\chi_2 = \dot{\chi}_3/\chi_3$.

4.3.2 Unit Cell Boundary Conditions

To enforce the assumption of a periodic array of unit cells, the faces of the unit cell must remain straight and move as rigid planes during the deformation process so that the cell remains cylindrical. The faces of the cell at $r = L_r$ and $z = L_z$ must have normal displacements and retain their mutual orientations. This condition is easily accomplished for one-quarter 2-D unit cell by designating the upper-right corner node as a master node denoted as 'A' in Fig. 4.6 to control the displacements of the radial and axial planes by using multipoint constraints. These constraints enable the lengths of the unit cell to be defined at an arbitrary state as

$$L_r = L_{r0} + u_r^{\mathrm{A}} \quad L_z = L_{z0} + u_z^{\mathrm{A}} \tag{4.22}$$

The formal displacement boundary conditions of the one-quarter unit-cell geometry are stated as

$$
\begin{array}{llll}
u_r = 0 & \text{along the axis} & r = 0, & 0 \le z \le L_z \\
u_z = 0 & \text{on the bottom} & 0 \le r \le L_r, & z = 0 \\
u_r = u_r^{\mathrm{A}} & \text{on the lateral surface} & r = L_r, & 0 \le z \le L_z \\
u_z = u_z^{\mathrm{A}} & \text{on the top} & 0 \le r \le L_r, & z = L_z
\end{array}
\tag{4.23}
$$

The boundaries of the cell are free of shear tractions and the surfaces of the void are free of all tractions. Additionally, the matrix material is assumed to be a pure matrix containing no secondary voids or particles. A void nucleation rule governing the formation of secondary voids is not considered because the unit cell results would be dependent upon that specific nucleation model and its assumed parameters. The above conditions are applicable to all of the void geometries and stress states considered in this chapter.

4.3.3 Stress State and Microstructure Evolution

The microscopic stress and strain tensors describe the stress state within the unit cell and are denoted by σ_{ij} and ε_{ij}. The macroscopic stress and strain tensor are applied at the cell boundaries and are denoted as Σ_{ij} and E_{ij}, respectively. Since the cell surfaces are free of shear, the applied stress and strain directions coincide with the principal directions. The macroscopic principal and equivalent strains are given as

$$E_{\mathrm{r}} = \ln\left(1 + \frac{u_r^{\mathrm{A}}}{L_{r0}}\right) \quad E_{\mathrm{z}} = \ln\left(1 + \frac{u_z^{\mathrm{A}}}{L_{z0}}\right) \quad E_{\mathrm{eq}} = \frac{2}{3}|E_z - E_r| \tag{4.24--4.26}$$

The remote true macroscopic principal stresses are calculated at any instant as the average reaction force at the cell faces per current area through

$$\Sigma_r = \frac{1}{L_z}\int_0^{L_z} S_r|_{r=L_r}\,dz \quad \Sigma_z = \frac{2}{L_r^2}\int_0^{L_r} rS_z|_{z=L_z}\,dr \qquad (4.27, 4.28)$$

where S is the stress vector. The corresponding macroscopic hydrostatic stress, Σ_{hyd}, equivalent stress, Σ_{eq}, and stress triaxiality, T, are calculated as

$$\Sigma_{hyd} = \frac{\Sigma_1 + \Sigma_2 + \Sigma_3}{3} \quad \Sigma_{eq} = |\Sigma_z - \Sigma_r| \quad T = \frac{\Sigma_{hyd}}{\Sigma_{eq}} \qquad (4.29\text{--}4.31)$$

The analysis can be simplified by defining a loading parameter, α, that can be determined for a specified stress triaxiality as

$$\alpha = \frac{\Sigma_r}{\Sigma_z} = \frac{3T - 1}{3T + 2} \qquad (4.32)$$

where $\alpha = 0$ for uniaxial tension ($T = 1/3$) or -0.5 for pure shear ($T = 0$). The plastic strain increment, $\dot{\varepsilon}^p$, and flow stress, $\bar{\sigma}$, within the unit cell can be determined from work equivalence as

$$\dot{\varepsilon}^p = \frac{\Sigma_{ij}\dot{E}_{ij}^p}{\bar{\sigma}(1-f)} \qquad (4.33)$$

by neglecting the elastic strains and assuming an incompressible matrix so that $\dot{E}_{ij}^p \approx \dot{E}_{ij}$. The microscopic plastic strain and flow stress of the unit cell are related by the stress-strain relation of the matrix. In the present study, the ductile matrix is assumed to be an isotropic, rate-independent material that hardens according to the power-law relation

$$\frac{\bar{\sigma}}{\sigma_y} = \left(1 + \frac{E}{\sigma_y}\bar{\varepsilon}^p\right)^n \qquad (4.34)$$

where σ_y is the initial yield stress, E is the Young's modulus and n is the hardening exponent. A typical value of $E/\sigma_y = 500$ is valid for most ductile engineering alloys where n varies from 0 to 0.40.

The void volume fraction of the unit cell can be computed from the updated coordinates of the element nodes that define the surface of the void or from an approximate analytical formula proposed by Koplik and Needleman (1988) using the cell volume, V, as

$$f = 1 - (1 - f_0)\left(\frac{V_0}{V} - \frac{3(1-v)}{E}\Sigma_{hyd}\right) \quad \frac{V}{V_0} = \frac{(L_{r0} + u_r^A)^2(L_{z0} + u_z^A)}{L_{r0}^2 L_{z0}} \qquad (4.35)$$
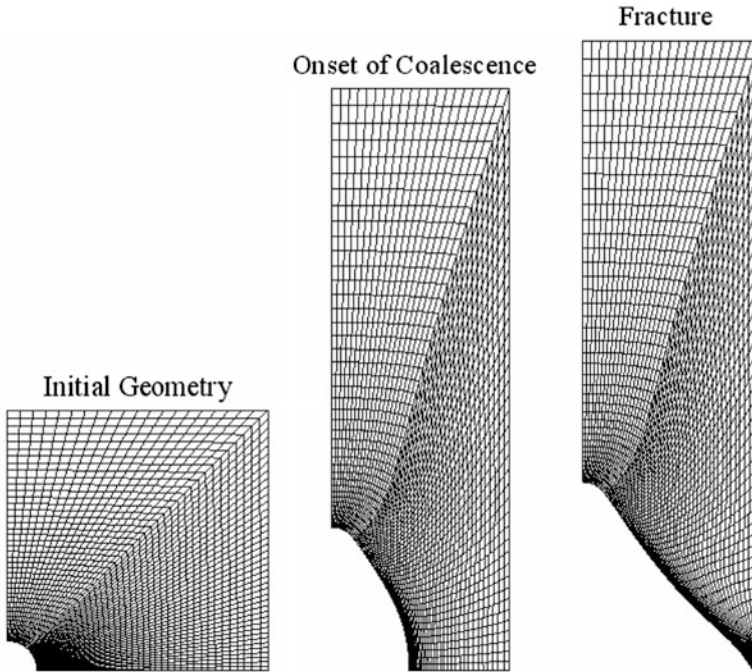
Fig. 4.7 Typical deformation history of a voided unit cell. Initially, the deformation mode is homogeneous and characterized by stable void growth until the onset of coalescence when the deformation mode becomes unstable and localized within the ligament. Note the abrupt change in the transverse growth of the void during coalescence compared to the vertical displacement of the cell. These results were obtained for an initially spherical void with an initial porosity of 0.1 % and subjected to a stress triaxiality of unity

This approximation provides very good agreement with numerical integration of the void surface as observed in previous studies (Koplik and Needleman 1988; Pardoen and Hutchinson 2000; Siad et al. 2008) and reduces the amount of post-processing. It should be noted that this approximation in Eq. (4.35) is not valid for a porous matrix material (secondary voids). The void aspect ratio, cell aspect ratio and the void spacing ratios can be readily determined from the geometry using Eqs. (4.2–4.5).

4.3.4 Identification of Void Coalescence

The termination of homogeneous deformation within the unit cell is marked by the onset of void coalescence when deformation becomes unstable and localized within the inter-void ligament while the material outside the ligament unloads elastically as shown in Fig. 4.7. The transition to void coalescence is identified by the radial strain rate approaching 0 as the unit cell deforms in a type of uniaxial stretching
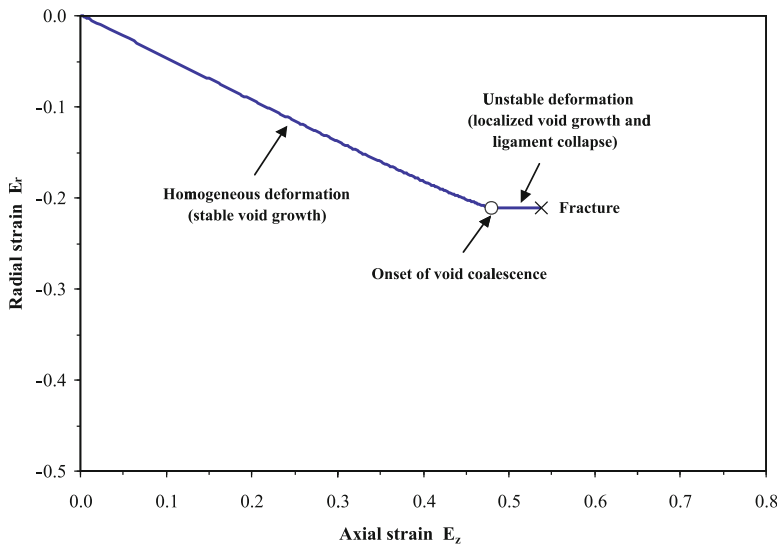
Fig. 4.8 Typical relationship of the macroscopic radial and axial strains for a voided unit cell. The onset of void coalescence is identified when the radial strain rate is 0

mode, regardless of the stress triaxiality. In this regime, the void expands rapidly in the transverse direction as the ligament length approaches 0 and the load-bearing capacity of the material is lost. Physically, this represents the collapse of the ligament as the void is beginning to link-up with a neighbouring void from an adjacent unit cell to form a larger void. However, in the finite-element simulation, the ligament will shrink and become highly deformed as the length approaches 0, ultimately requiring a re-meshing scheme to model the post-coalescence regime.

In the present study, the finite-element simulations are terminated after the onset of void coalescence as the results of the model in the post-coalescence regime are not of prime importance. For the practical range of stress triaxiality found in sheet metal forming operations $(T \leq 1)$, the collapse of the ligament occurs almost instantaneously and thus the coalescence strain can be used as an excellent approximation to the fracture strain. The procedure for identifying the onset of coalescence using the radial strain rates is demonstrated in Fig. 4.8 and the associated loss of load-bearing capacity with coalescence is illustrated in Fig. 4.9.

4.3.5   Numerical Solution Procedure

To obtain general trends for damage evolution and coalescence within a unit cell, the stress triaxiality must be kept constant throughout the cell during deformation. Since the compressibility of the cell varies during deformation, the stress triaxiality will steadily increase and fluctuate unless a control scheme is used to adjust the displacements of the cell faces. This problem becomes acute near the onset of void
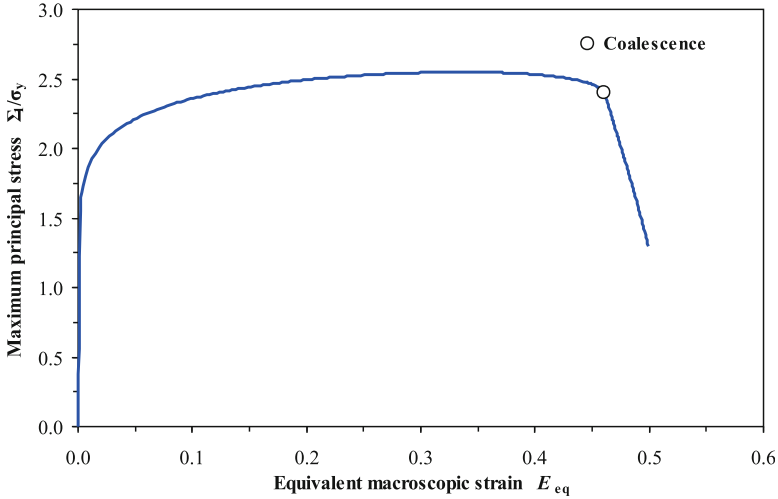
Fig. 4.9 Typical macroscopic stress and strain curve for a voided unit cell. Note that the loss of load-bearing capacity of the material is approximately linear in the post-coalescence regime

coalescence where deformation becomes unstable within the inter-void ligament. Fortunately, using ABAQUS finite-element software, the modified Riks-algorithm (Riks 1979) is ideally suited to incrementing the load on the unit cell to maintain equilibrium. The Riks method is an iterative scheme that allows equilibrium solutions to be found for nonlinear, unstable problems such as buckling or an abrupt change in the deformation mode such as a snap-through process or void coalescence.

The Riks-option within ABAQUS is employed to determine the displacements on the unit cell faces in such a way to enforce the loading parameter, α, in Eq. (4.32) to be a constant prescribed value based upon the specified stress triaxiality. The axial stress, Σ_z, is set to unity and the corresponding radial stress is $\Sigma_r = \alpha$. Consequently, the axial direction is the principal loading direction for all simulations in the present study since $\alpha < 1$ for the range of stress triaxialities considered ($1/3 \leq T \leq 3$). Convergence studies were performed to test for mesh dependence and it was found to be minimal if the element shape within the ligament is rectangular and the mesh is sufficiently refined near the void surface as seen in Figs. 4.5 and 4.7. The accuracy of the unit cell results was verified through comparison with previous cell studies in the literature by Pardoen and Hutchinson (2000), Lassance et al. (2006) and Scheyvaerts et al. (2010).

4.4   Unit Cell Simulation Results

A large number of finite-element models have been developed with an emphasis placed on small void aspect ratios ($W < 1$) that best resemble the conditions observed in particle cracking and debonding. Typical void shape evolution models

are only valid for an aspect ratio greater than 1/6 while voids nucleated by particle cracking have an aspect ratio close to 0. Knowledge of the deformation of the void at small aspect ratios is critical since many alloys nucleate voids by particle cracking. To best represent an isolated void within a real material the initial porosity of the voids is taken to be 0.01 and 0.1 %. Smaller porosities could be considered with the use of an adaptive remeshing algorithm since very large strains would be required to grow the void to coalescence. Finally, the simulations are terminated shortly after the onset of coalescence as mesh distortion effects become significant, especially for initially flat voids. Fortunately, the load drop, the void growth rate and shape evolution all become linear within the post-coalescence regime and their behaviour can be reliably extrapolated to estimate their value at fracture (Scheyvaerts et al. 2010).

The aspect ratios considered in the analysis are: 0.001, 0.01, 0.05, 1/6, 1 and 6 for porosities of 0.1 and 0.01 % for a general hardening exponent of 0.10. To enable the results to be generalized to any material, the parameters in the flow stress relation for the material in Eq. (4.34) are $E/\sigma_y = 500$, which is applicable to a wide range of engineering materials (Pardoen and Hutchinson 2000). The stress triaxialities range from 1/3 to 3 to capture void evolution in stress states ranging from uniaxial tension to the severe conditions found ahead of a crack tip. It is important to note that the stress states considered are purely triaxial and that no shear stress is present. The influence of shear on void growth and shape evolution is currently a very active area of research and complex boundary conditions are required to enforce a constant stress state. The interested reader is referred to Barsoum and Faleskog (2007a, b) and Scheyvaers et al. (2010) for further information.

4.4.1 Penny-Shaped Voids: $W_o = 1/100$

The evolution of the porosity and the aspect ratio of an initially penny-shaped void for a wide range of stress triaxialities are presented in Figs. 4.10 and 4.11, respectively. What is most remarkable about these figures is that the voids grow exceedingly fast and in an approximately linear fashion in each stress state. In uniaxial tension ($T = 1/3$), the void enlarges from 0.1 % to nearly 9 % while the aspect ratio changes by a factor of over 100 and is roughly spherical at fracture. The linear nature of the penny-shaped voids evolution is attributed to it opening in the load direction and experiencing negligible lateral growth. As most nucleated voids are initially penny-shaped, the proper modeling of this geometry is of prime importance for modelling damage in alloys where void nucleation is significant as in the 5xxx series Al-Mg alloys (Chen 2004; Orlov 2006; Butcher 2011).

The rapid expansion of initially penny-shaped voids is an interesting result since SEM micrographs commonly observe spherical dimples that are indicative of ductile fracture as shown in Fig. 4.12. During the final stage of ductile fracture, the high stress triaxiality surrounding the primary voids nucleates voids from the
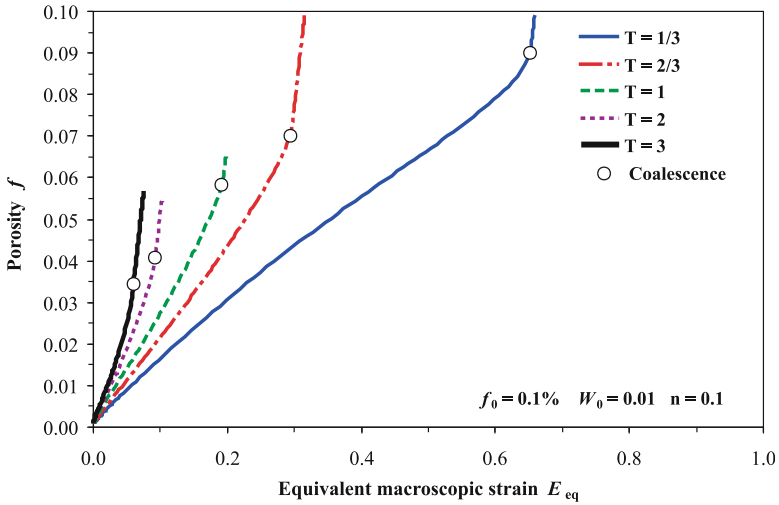
Fig. 4.10 Porosity history of a penny-shaped void subjected to various triaxial loadings
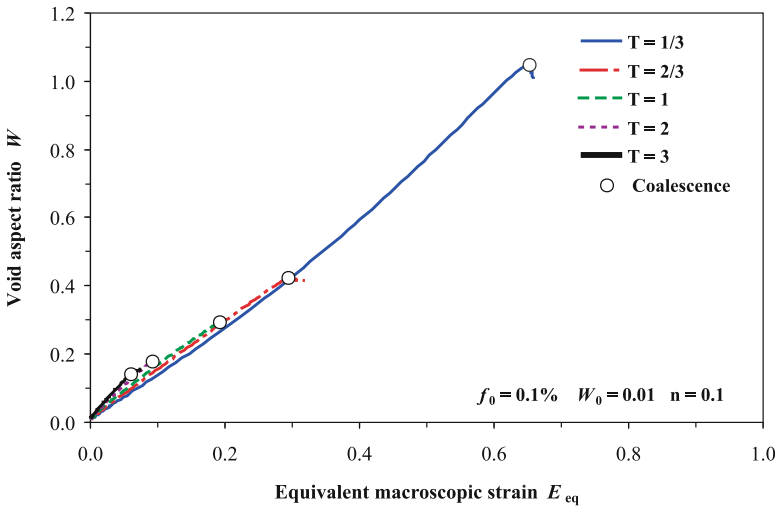
Fig. 4.11 Evolution of the void aspect ratio of an initially penny-shaped void subjected to various triaxial loadings

surrounding particles and the rapid growth of these penny-shaped voids can explain the spherical-shaped voids on the fracture surface. The high stress triaxiality will also encourage pre-existing voids to grow in a spherical manner and may even cause prolate voids to turn into oblate voids if the value is high enough.

Fig. 4.12 SEM micrograph of the fracture surface in an AA5182 alloy. Note the presence of the smaller secondary dimples surrounding the dimple from a primary void in the top of the figure
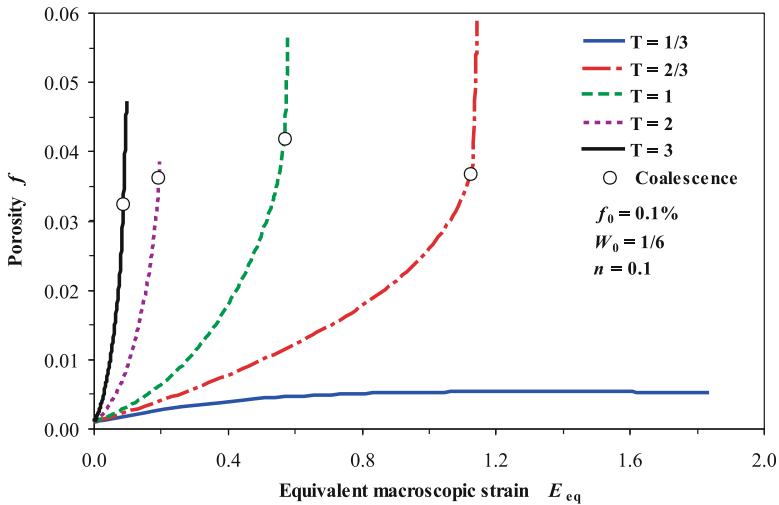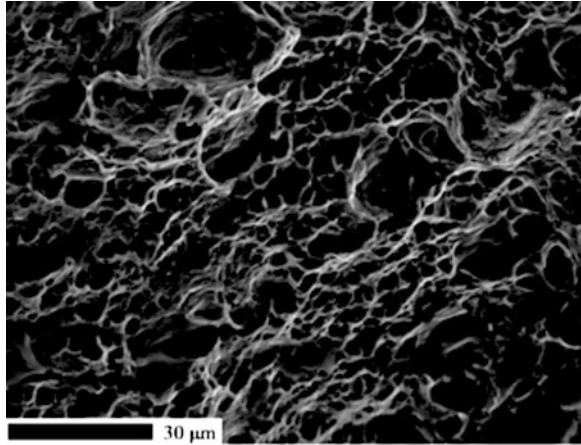
Fig. 4.13 Porosity history of an initially oblate void subjected to various triaxial loadings

4.4.2 Oblate Voids: $W_o = 1/6$

The growth and shape evolution of an initially oblate void is presented in Figs. 4.13 and 4.14, respectively. The expected non-linear response of the voids begins to emerge where void growth is slow at low triaxiality and rapid at high triaxiality. The high growth rate at high large stress triaxiality occurs because the void has sufficient height to be expanded by the lateral stress. This is in contrast with the

Fig. 4.14 Shape evolution of an initially oblate void subjected to various triaxial loadings

initially penny-shaped void whose growth rate is nearly linear and much less sensitive to the hydrostatic stress.

Conversely, in uniaxial tension, the void becomes prolate and the void growth rate is very slow compared to the penny-shaped case. Prolate voids do not grow significantly at low triaxiality because plastic flow of the material over the void surface becomes easier as the voids laterally contract and become needle-like. In the limit, the void essentially closes and the matrix can deform almost as if the void were not present.

4.4.3 Spherical Voids: $W_o = 1$

The well-known void evolution trends for spherical voids are presented in Figs. 4.15 and 4.16. The void growth trends for spherical voids are similar to that of the oblate void with the difference in the growth rates between stress states more exaggerated. The trend for the aspect ratio shows a new development compared to the previous cases in that the void becomes oblate at high stress triaxiality. The height of the void is sufficiently large for the hydrostatic stress at high triaxiality to cause the void to grow laterally and cause the aspect ratio to decrease despite the principal loading direction being vertical. This is a counterintuitive but well documented phenomenon for voids at high stress triaxiality and highlights the difficulties in developing a shape evolution model because the void grows laterally when one would expect it to grow axially.

Fig. 4.15 Porosity history of an initially spherical void subjected to various triaxial loadings
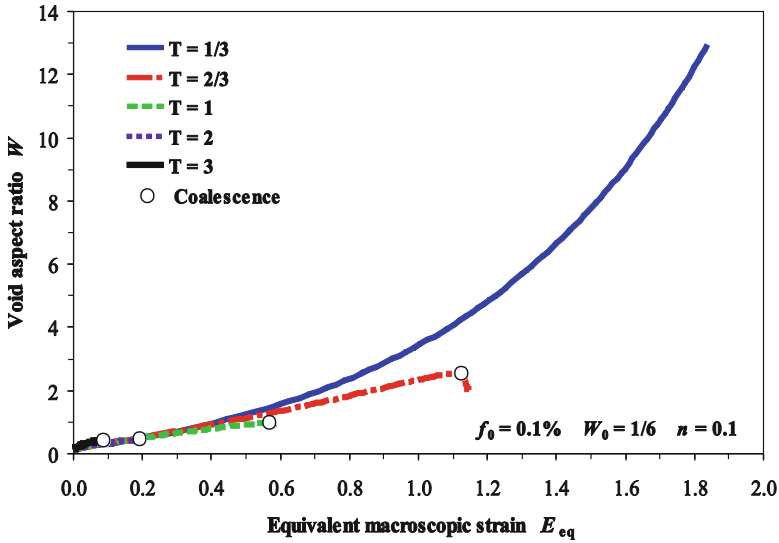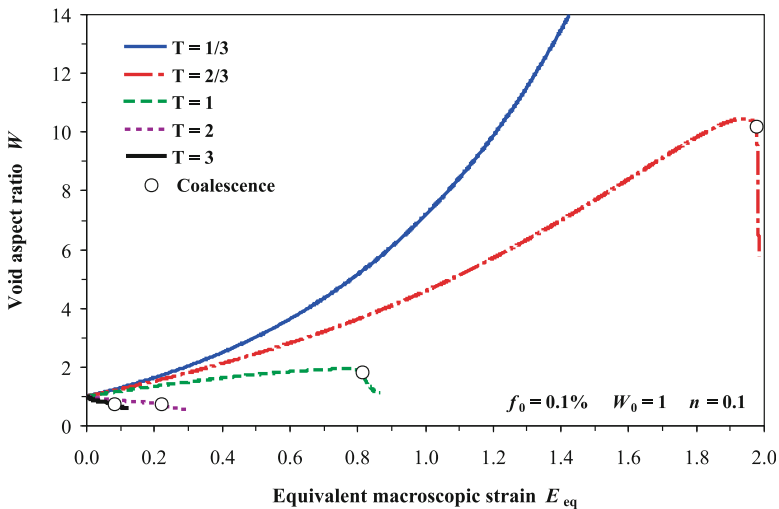

Fig. 4.16 Shape evolution (*right*) of an initially spherical void subjected to various triaxial loadings

4.4.4   Prolate Voids: $W_o = 6$

Finally, the void growth and shape evolution for initially prolate voids are presented in Figs. 4.17 and 4.18. The trends are again similar to the spherical case with the influence of the stress state more dramatic. What is most apparent is that the growth of the voids is completely negligible in uniaxial tension as the void becomes extremely
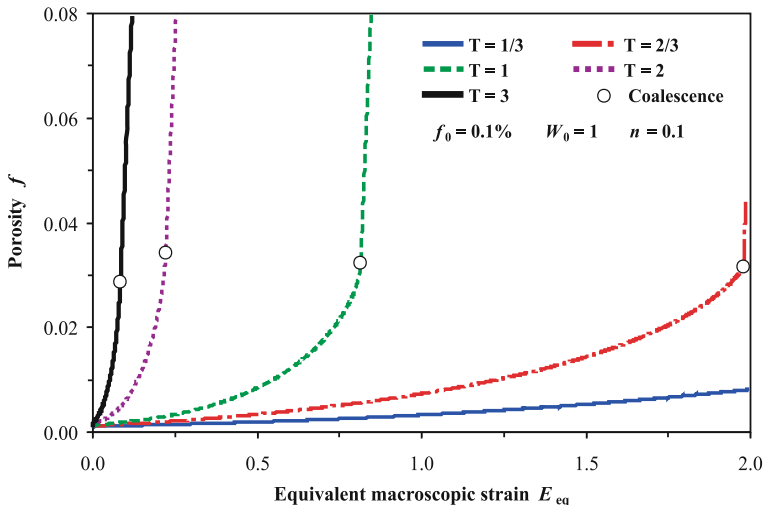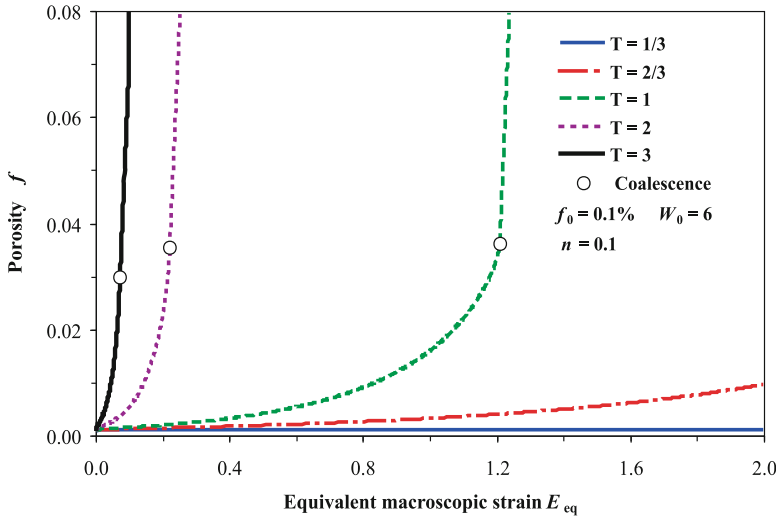
Fig. 4.17 Porosity history of an initially prolate void subjected to various triaxial loadings
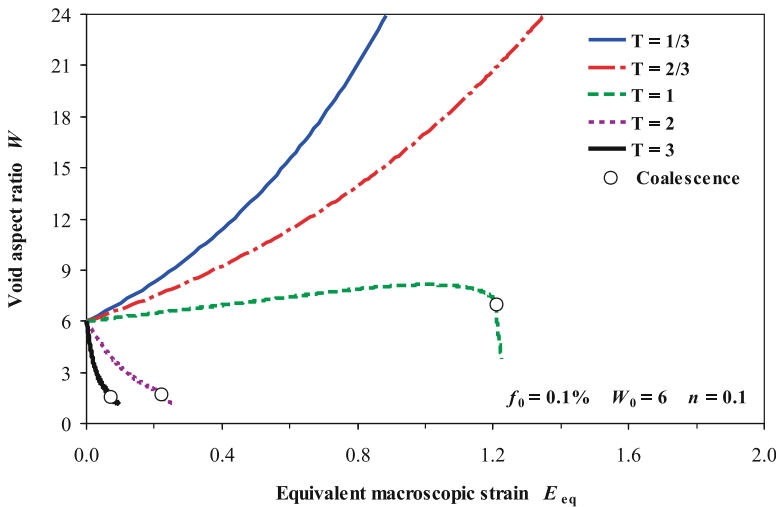
Fig. 4.18 Shape evolution of an initially prolate void subjected to various triaxial loadings

prolate but occupies nearly the same volume. Void growth remains very low at a triaxiality of 2/3 which corresponds to equal-biaxial tension. Since the void is initially prolate and much taller than it is wide, it is very susceptible to lateral growth at high triaxiality and the void shape becomes nearly spherical at fracture. From a modeling perspective, prolate voids are not of paramount importance since their growth rates are so small in the practical regime found in metal forming ($T < 1$).
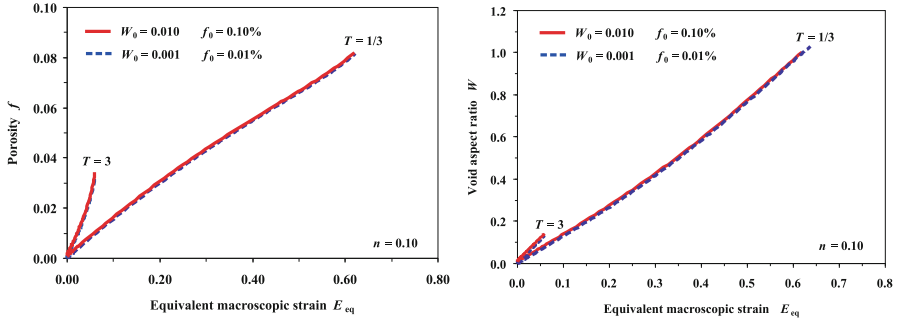
Fig. 4.19 Comparison of void growth and shape evolution for different penny-shaped voids for the extreme cases for the stress triaxiality

4.4.5   Selection of a Minimum Void Aspect Ratio

There are only so many finite-element simulations and unit cell geometries one can consider and the argument can always be made for why different stress states or geometries should have been included. Overall, a maximum initial aspect ratio of 6 seems reasonable for the modeling of prolate voids since most voids will be nucleated by particle cracking and debonding and best described as penny-shaped. If penny-shaped cracks are the most important void geometry then what is the minimum shape that can be considered? In the limit, the penny-shaped void has no initial height, the aspect ratio is 0, and it cannot be modeled using regular finite-element techniques. Mesh distortion issues also arise when modeling increasingly small voids so there is a practical limit to the geometry one can consider.

Fortunately, the void growth rate and shape evolution for extremely flat voids are essentially the same as shown in Fig. 4.19, which is caused by deformation primarily occurring in the opening direction of the void. The void opens in the loading direction at a high enough rate that the solutions for aspect ratios of 1/1,000 and 1/100 are quite similar. This is an extremely fortuitous result since any void that is nucleated by particle cracking can be assigned an arbitrary aspect ratio of 0.01, removing a parameter that otherwise would have had to been predetermined. A similar result has also been reported by Lassance et al. (2006).

4.5   Theoretical Models for Void Growth, Shape and Coalescence

With the benchmark trends for void growth and shape evolution established, the validity of the analytical evolution models can be evaluated. It is important to state that these models are all expected to perform at least reasonably well in some stress states, or they would be without merit in the first place. However, it is of great

practical interest to evaluate the performance of these models in a variety of conditions to establish confidence in the model predictions for a wide range of stress states.

4.5.1   Yield Criterion

The yield criterion of Gurson and Tvergaard (GT) described in Eq. (1.23) is adopted to describe material softening and will be used to integrate the stress state in the analytical model. The extension of Ragab (2004a) is adopted to account for the influence of the void shape in the GT model. In this extension, q_1 and q_2 parameters in the yield function are no longer material constants but related to the stress state, void shape and material hardening.

4.5.2   Void Growth, Shape Evolution and Coalescence

Due to the large number of void shape growth and shape evolution models available in the literature, it is prohibitive to evaluate all of them since they are all valid for certain situations. Fortunately, the semi-empirical void growth and evolution models of Ragab (2004a) provide a logical and reasonable benchmark. Ragab (2004a) developed and validated a set of semi-empirical equations by performing a large-scale meta-analysis of the definitive analytical and numerical studies of void growth and shape evolution in the literature (McClintock 1968; Rice and Tracey 1969; Budiansky et al. 1982; Huang 1991; Lee and Mear 1992a, b; Yee and Mear 1996; Sovik and Thaulow 1997; Pardoen and Hutchinson 2000). In his analysis, Ragab (2004a, b) individually calibrated the q_i parameters in the GT yield criterion as functions of the void shape, porosity, stress state and hardening exponent. The calibrated (q_1, q_2) parameters not only enabled improved modelling of an isolated void but also improve the accuracy of the yield criterion by accounting for void shape effects while preserving the relatively simple Gurson framework. This is very advantageous since other damage-based models such as the GLD model and its variants (Gologanu et al. 1997; Benzerga 2002) that account for void shape effects are more cumbersome to implement compared to the GT model. An approximate method for estimating the influence of the void shape on the yield criterion is preferable to implementing these rigorous models.

It is important to note that the semi-empirical equations of Ragab (2004a) were not derived directly from finite-element simulations of a voided unit cell but from a large range of published analytical and numerical data for a large range of void geometries, stress states and material hardening exponents. As a result, it is of interest to directly compare the final equations with the finite-element simulations to best evaluate their performance. Butcher (2011) performed a large-scale finite-element

study of cylindrical unit cells with void shapes ranging from penny-shaped to prolate to validate the Ragab (2004a, b) void growth and shape evolution models.

4.5.2.1 Void Growth

The associated flow rule of the GT model can be employed to obtain an alternate expression for the void growth rate using the first principal strain rate:

$$\dot{f}_{\text{growth}} = \frac{3f(1-f)q_1 q_2 \sinh\left(q_2 \frac{3}{2} \frac{\Sigma_{\text{hyd}}}{\bar{\sigma}}\right)}{3\left(\frac{\Sigma_1 - \Sigma_{\text{hyd}}}{\bar{\sigma}}\right) + fq_1 q_2 \sinh\left(q_2 \frac{3}{2} \frac{\Sigma_{\text{hyd}}}{\bar{\sigma}}\right)} \dot{E}_1^{\text{p}} \tag{4.36}$$

and simplified by Ragab (2004a) by assuming small porosities and axisymmetric deformation to obtain

$$\frac{\dot{f}_{\text{growth}}}{f} = \frac{3}{2} q_1 q_2 \sinh\left(q_2 \frac{3}{2} \frac{\Sigma_{\text{hyd}}}{\bar{\sigma}}\right) \dot{E}_1^{\text{p}} \tag{4.37}$$

that was then calibrated to the void growth results available in the literature.

The semi-empirical equations of Ragab (2004a) for the variation of the q_i parameters in the GT model are valid for a large range of stress triaxiality from $1/3 \leq T \leq 8/3$, and for hardening exponents up to 0.40. The q_i relations are

$$q_1 = A + BT + CT^2 + DT^3$$
$$A = 2.28 - 3.55n + 3.84n^2 \quad B = -0.92 + 1.32n - 0.32n^2$$
$$C = 0.53 - 2.31n + 2.35n^2 \quad D = -0.10 + 0.27n + 0.70n^2 - 1.78n^3 \tag{4.38}$$

$$q_2 = W^{\eta}$$
$$\eta(W < 1) = 0.206 \ln(T) - 0.266 - 0.02n$$
$$\eta(W \geq 1) = -3.484 + 11.614T - 13.72T^2 + 6.54T^3 - 1.06T^4 + 0.2n \tag{4.39}$$

4.5.2.2 Void Shape Evolution

For a constant strain-path, the evolution law of Ragab (2004a) for the void aspect ratio is

$$\ln(W/W_0) = 1.1(\omega + 2 - \Sigma_{\text{hyd}}/\bar{\sigma} + n)(1 - f_0)E_{\text{eq}}^{\text{p}} \tag{4.40a}$$

Fig. 4.20 Comparison of the analytical void shape evolution model with the unit cell data for an initially penny-shaped void

Where ω is defined for initially oblate $(1/6 \leq W_0 \leq 1)$ and prolate voids $(1 \leq W_0 \leq 6)$ as

$$\omega_{\text{oblate}} = -\ln(W_0) \Big/ \left(0.109 + 1.224E_{\text{eq}}^{\text{p}}\right)$$

$$\omega_{\text{prolate}} = \left(-0.535 + 0.0235E_{\text{eq}}^{\text{p}}\right)\ln(W_0) \qquad (4.40\text{b, c})$$

4.5.3   Comparison with Unit Cell Results

4.5.3.1   Void Shape

The predictions of the semi-empirical model of Ragab (2004a) for the void aspect ratio for the range of initial shapes considered are presented in Figs. 4.20 through 4.23. Unlike the void growth model, the predictions for the initial penny-shaped void in Fig. 4.21 are in very good agreement with the unit cell data. This is a surprising result since the model was not calibrated for this regime. Overall, the model gives decent predictions for the void aspect ratio for oblate, spherical and prolate voids in most stress states. The predictions are the least accurate in the case of prolate voids but the accuracy is reasonable at low strains, say, of 0.30. This is not a significant limitation since initially prolate voids with an aspect ratio of 6 are not as common as initially penny-shaped or oblate voids since these shapes best resemble the void at nucleation by particle cracking and partial debonding. In
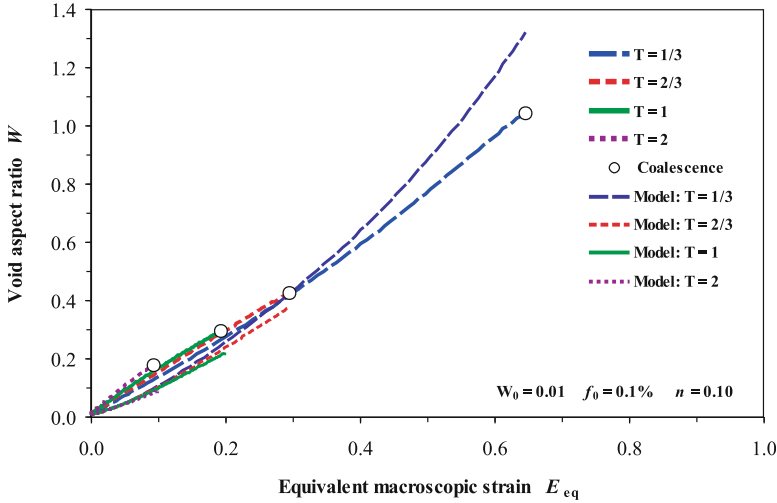
Fig. 4.21 Comparison of the analytical void shape evolution model with the unit cell data for an initially oblate void

general, the shape evolution model is quite reasonable and suitable for use in a typical damage-based constitutive model and is very attractive for its simplicity.

4.6   Calibration of the Void Evolution Models

4.6.1   Void Growth

The void growth model of Ragab (2004a) used a simplified version of the growth rule obtained for the Gurson model. In the present work, we will use the original form of the growth rule in Eq. (4.36) because unlike Ragab (2004a), the unit cell data has been obtained first-hand and not taken from the literature. The q_2 parameter cannot be solved for explicitly in Eq. (4.36) and a Newton-Raphson method is used to determine the q_2 value obtained at each time-step in the unit cell simulation. The calibrated q_2 values for each void geometry and stress state were determined to create a library of highly accurate void growth correlations in Table 4.1. The calibrated q_2 values for several of the void shapes considered are shown in Fig. 4.24. The calibrated q_2 value converges to a value of unity for a spherical void which is the value derived by Gurson (1975). The calibrated void growth model is compared with the unit cell data in Fig. 4.25 and the agreement is excellent.
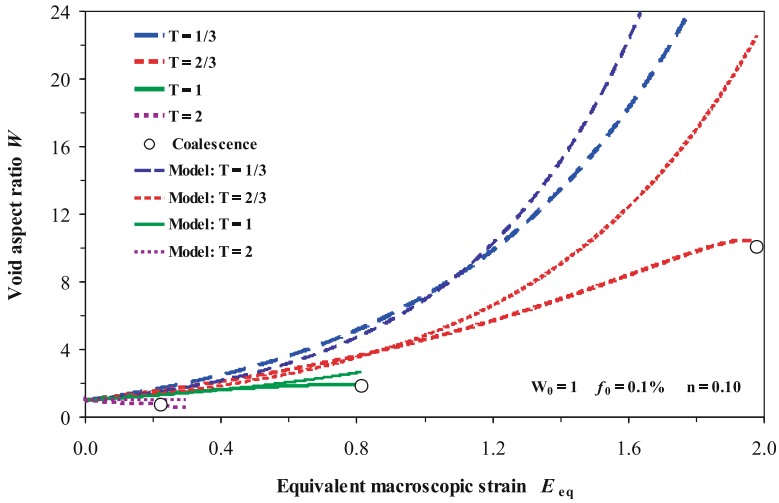
Fig. 4.22 Comparison of the analytical void shape evolution model with the unit cell data for an initially spherical void
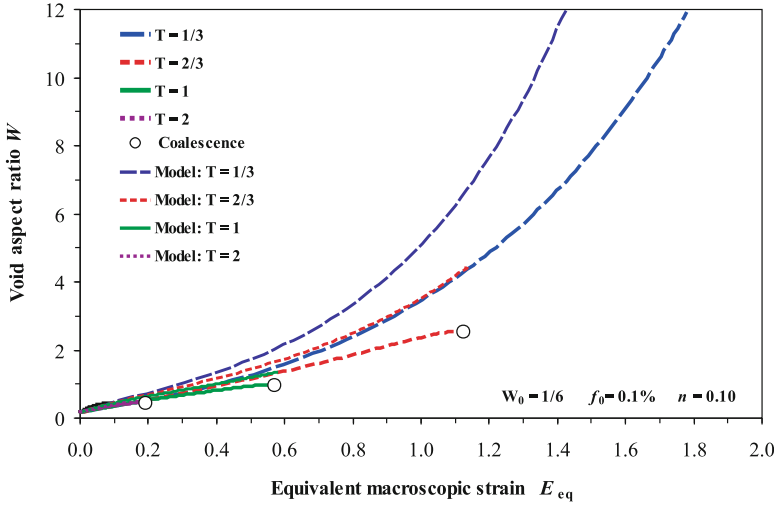

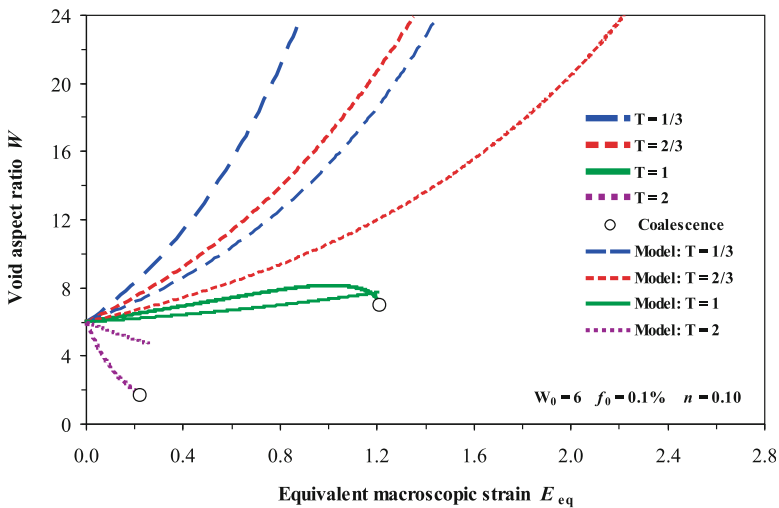**Fig. 4.23** Comparison of the analytical void shape evolution model with the unit cell data for an initially prolate void

4.6.2   Void Shape Evolution

Although the semi-empirical equations of Ragab (2004a) give pretty good results for the void aspect ratio, a calibration is required because void growth is tightly coupled to the void shape through $q_2 = W^{\eta}$. Due to this exponential dependence, the

Table 4.1 Void growth calibration parameters for various void volume fractions, void shapes and stress triaxiality ratios

f_o (%)	W_o	T	ζ	Range of the aspect ratio (W) that correlation is valid		Range of the equivalent strain (ε_{eq}) that correlation is valid	
				W_o	W_{limit}	ε_o	ε_{limit}
0.1	0.01	1/3	−0.4310	0.01	1.00	0	0.62
		2/3	−0.3150		0.42		0.29
		1	−0.2530		0.29		0.19
		2	−0.2081		0.18		0.09
		3	−0.2310		0.14		0.06
	0.05	1/3	−0.4785	0.05	1.00	0	0.50
			−0.7580	1.00	4.00	0.50	1.22
		2/3	−0.3300	0.05	1.00	0	0.51
			−0.1200	1.00	1.36	0.52	0.71
		1	−0.2440	0.05	0.69	0	0.40
		2	−0.1170		0.36	0	0.15
		3	−0.3210		0.31	0	0.08
	1/6	1/3	−0.5850	1/6	1.00	0	0.41
			−0.8879	1	6.00	0.41	1.33
		2/3	−0.3600	1/6	0.97	0	0.41
			−0.3000	1	2.39	0.43	1.01
		1	−0.2350	1/6	0.98	0	0.57
		2	−0.0850		0.47		0.19
		3	−0.1120		0.45		0.09
	1	1/3	−0.0700	1	33.25	0	2.00
		2/3	−0.1695		10.46		1.94
		1	−0.0780		1.94		0.76
		2	−0.0580		0.75		0.22
		3	−0.6290		0.59		0.12
	6	1/3	−0.6030	6	27.07	0	0.97
		2/3	−0.1900		17.97		1.06
		1	−0.0980		8.14		1.00
		3	0.0850		1.81		0.06
	0.001	1/3	−0.4045	0.001	1.00	0	0.62
		2/3	−0.3100		0.42		0.30
0.01		1	−0.2540		0.29		0.19
		2	−0.2180		0.17		0.09
		3	−0.2320		0.13		0.06
	1	1/3	−0.8881	1	35.43	0	2.03
		2/3	−0.7000		7.03		1.37
		1	−0.0890		2.14		1.06
		2	−0.2200		0.62		0.30
		3	−0.4140		0.71		0.11
	6	1/3	−0.1200	6	147.72	0	2.09
		2/3	−0.1240		39.03		1.84
		1	−0.0960		9.30		1.50
		2	0.0330		1.02		0.31
		3	0.1200		1.03		0.10

(continued)

Table 4.1 (continued)

f$_o$ (%)	W$_o$	T	ζ	Range of the aspect ratio (W) that correlation is valid		Range of the equivalent strain (ε$_{eq}$) that correlation is valid	
				W$_o$	W$_{limit}$	ε$_o$	ε$_{limit}$
	1/6	1/3	−0.5180	1/6	1.02	0	0.47
			−0.5200	1	2.57	0.47	0.98
1		2/3	−0.3260	1/6	0.83	0	0.42
		1	−0.2210		0.53		0.25
		2	−0.1970		0.34		0.10
		3	−0.2920		0.28		0.05
	1	1/3	−0.7200	1	9.22	0	1.21
		2/3	−0.3100		3.52		0.85
		1	−0.1900		1.59		0.41
		2	−0.5000		0.88		0.13
		3	−5.8000		0.84		0.04
	6	1/3	−0.6750	6	137.63	0	2.05
		2/3	−0.1750		21.27		1.20
		1	−0.1050		7.30		0.64
		2	0.0050		2.95		0.14
		3	0.3410		3.29		0.04

A piece-wise correlation is used for certain void shapes at low triaxialities and the ranges that the calibration parameters are accurate are given for both the void shape and equivalent strain
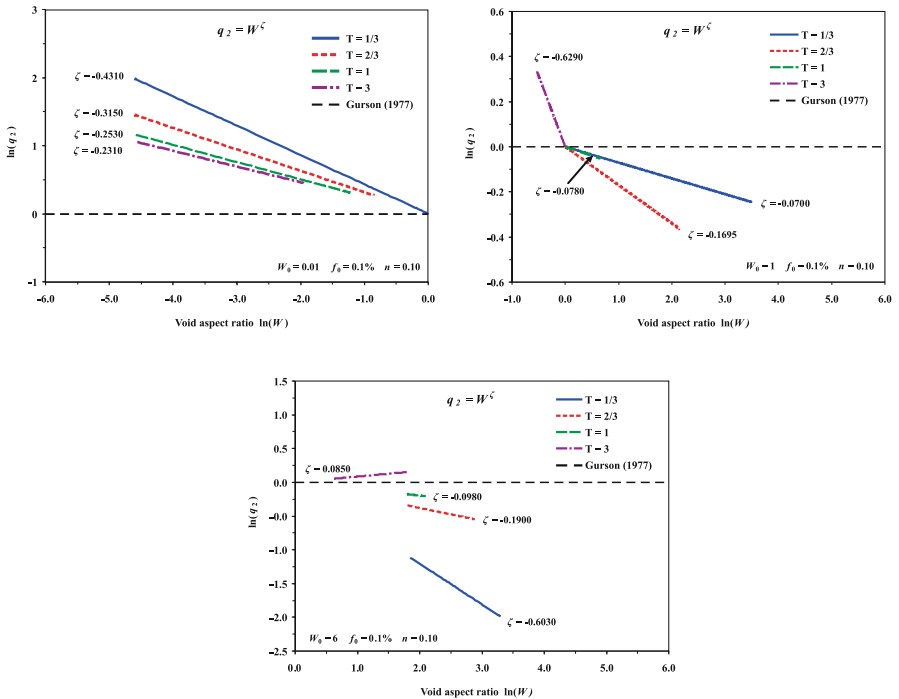

Fig. 4.24 Calibrated q2 parameter for an initially penny-shaped void (*top-left*), spherical void (*top-right*) and prolate void (*center*) subjected to various stress triaxialities
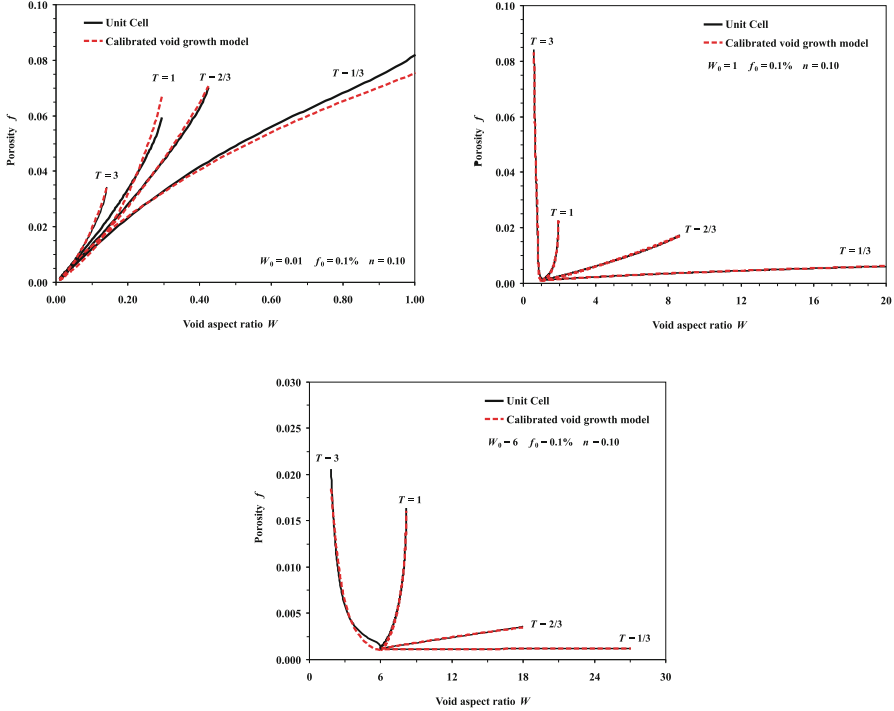
Fig. 4.25 Comparison of the calibrated void growth model with the unit cell data for an initially penny-shaped (*top-left*), spherical (*top-right*) and prolate void (*center*)

previous void growth calibration is in vain unless the aspect ratio is also highly accurate because errors in the aspect ratio will be magnified in the growth rule. Unlike the growth rule, the semi-empirical equation for the void shape is a pure correlation and its form is not readily amenable to calibration. To ensure that the void aspect ratio is modeled to a high degree of accuracy, a second-order polynomial was observed to be suitable to very large strains. If higher strains are required, the curve is linearly extrapolated with the slope selected to give good agreement to high strains. The correlation function for the aspect ratio is a function of the equivalent strain and initial aspect ratio as

$$
\begin{aligned}
W &= a_2 E_{\text{eq}}^2 + a_1 E_{\text{eq}} + W_{\text{o}} \quad E_{\text{eq}} \leq E_l \\
W &= b_1 \left(E_{\text{eq}} - E_l \right) + W_l \quad E_{\text{eq}} > E_l
\end{aligned}
\tag{4.41}
$$

where E_l is the limit strain and a_1, a_2, and b_1, are the calibration coefficients. W_l is the aspect ratio at the limit strain. For nearly all geometries considered, b_1 was selected so that it can be computed as the derivative of quadratic correlation evaluated at the limit strain. The calibrated parameters are presented in Tables 4.2, 4.3 and 4.4.

Table 4.2 Parameters for the void aspect ratio for an initial porosity of 0.01 % and a hardening exponent of 0.10

Aspect ratio	T	a_2	a_1	W_0	Limit strain ε_1	R^2	Aspect ratio at strain limit W_l	Slope for extrapolation b_l
0.001	1/3	0.68	1.19	0.00	0.635	1.000	1.031	2.114
	2/3	−0.25	1.49	0.00	−0.275	1.000	0.393	1.357
	1	−1.25	1.73	0.00	0.190	1.000	0.300	1.256
	2	−3.37	2.16	0.00	0.090	1.000	0.168	1.553
	3	−5.76	2.57	0.00	0.059	1.000	0.133	1.894
1/6	1/3	2.69	1.84	0.17	0.900	0.999	4.008	12.000
	2/3	1.14	1.34	0.17	1.800	1.000	6.278	5.450
	1	−0.51	1.94	0.17	0.850	1.000	1.448	1.072
	2	−7.61	2.95	0.17	0.140	1.000	0.431	0.821
	3	−66.36	9.68	0.17	0.063	0.998	0.513	1.316
1	1/3	3.51	2.34	1.00	0.800	1.000	5.115	11.000
	2/3	1.86	1.83	1.00	1.500	1.000	7.921	7.400
	1	−0.73	1.87	1.00	0.950	1.000	2.118	0.482
	2	2.67	−2.00	1.00	0.250	1.000	0.667	−0.664
	3	49.38	−7.04	1.00	0.063	0.994	0.753	−0.817
6	1/3	15.00	7.15	6.00	1.000	0.999	28.144	56.000
	2/3	6.37	4.89	6.00	1.500	0.999	27.672	24.007
	1	0.06	2.31	6.00	0.750	1.000	7.767	2.402
	2	65.28	−35.12	6.00	0.240	1.000	1.331	−3.785
	3	1547.53	−166.15	6.00	0.050	0.995	1.561	−11.397

The shaded values of b1 were manually adjusted and do not correspond to the derivative of the quadratic correlation

A limitation of the void shape evolution rule in Eq. (4.41) is that the initial void aspect ratio must be known and that it is not readily amenable to non-proportional loadings. However, it is compact, highly accurate and can be used to predict the void shape in uncoupled damage models where porosity-induced softening is minor and the void shape is only of interest for modelling coalescence. If a rate-based void shape evolution model is required, it is suggested to use the void shape evolution model from the GLD model or its variants (Pardoen and Hutchsinon 2000; Lassance et al. 2006; Scheyvaerts et al. 2010).

Care must be taken when calibrating the void aspect ratio because the trend for the aspect ratio departs from that of an isolated void prior to coalescence as shown in Fig. 4.26. Prior to coalescence, the void begins to interact with its neighbour, raising the local stress triaxiality and flattening the void. These interactions must be avoided during the calibration process as they are geometry dependent and the voids are assumed to be isolated. The limit strain in the correlation is selected to ensure interaction effects are avoided. The correlation functions for the different void geometries are compared with the unit cell data in Fig. 4.27, which shows that they accurately predict the aspect ratio to high strains while avoiding interaction effects.

Table 4.3 Parameters for the void aspect ratio for an initial porosity of 0.1 % and a hardening exponent of 0.10

Aspect ratio	T	a_2	a_1	W_0	Limit strain ε_1	R^2	Aspect ratio at strain limit W_l	Slope for extrapolation b_l
0.01	1/3	0.66	1.20	0.01	0.600	1.000	0.966	1.921
	2/3	−0.25	1.49	0.01	0.300	1.000	0.435	1.341
	1	−1.28	1.73	0.01	0.190	1.000	0.300	1.240
	2	−3.54	2.15	0.01	0.092	1.000	0.178	1.500
	3	−6.41	2.58	0.01	0.059	1.000	0.140	1.820
0.05	1/3	1.86	0.88	0.05	1.200	0.999	3.789	6.800
	2/3	0.27	1.70	0.05	0.500	1.000	0.966	1.968
	1	−1.01	2.01	0.05	0.400	1.000	0.693	1.203
	2	−5.54	2.83	0.05	0.130	1.000	0.324	1.388
	3	−26.80	5.42	0.05	0.075	0.999	0.305	1.419
1/6	1/3	2.07	1.17	0.17	1.200	0.993	4.552	6.144
	2/3	0.45	1.75	0.17	0.950	1.000	2.244	2.618
	1	−0.94	2.01	0.17	0.480	1.000	0.914	1.107
	2	−6.23	2.71	0.17	0.160	0.999	0.441	0.717
	3	−52.43	7.20	0.17	0.050	0.999	0.395	1.954
1	1/3	4.02	2.04	1.00	1.000	0.999	7.060	14.500
	2/3	1.62	2.01	1.00	1.750	1.000	9.484	7.690
	1	−0.85	1.92	1.00	0.750	1.000	1.957	0.637
	2	3.18	−1.72	1.00	0.180	1.000	0.794	−0.572
	3	48.87	−6.29	1.00	0.055	0.995	0.802	−0.914
6	1/3	14.9765	7.1021	6.00	1.100	0.999	31.934	62.000
	2/3	6.1131	5.0528	6.00	1.500	0.999	27.334	23.392
	1	−0.0903	2.4216	6.00	0.890	1.000	8.084	2.261
	2	69.2512	−33.6241	6.00	0.170	1.000	2.285	−10.079
	3	11.9209	−12.2347	6.00	0.070	1.000	5.202	−10.566

The shaded values of b1 were manually adjusted and do not correspond to the derivative of the quadratic correlation

4.6.3   Void Coalescence

It is of interest to evaluate the performance of the coalescence models since coalescence is predicted as a function of the void geometry. The coalescence model will only be as accurate as the sub-models that describe the void geometry. The models of Pardoen and Hutchinson (2000) and Benzerga (2002) in Eqs. (1.15) and (1.16) were evaluated using the geometry of the voids from the unit cell simulations to obtain their predictions under ideal conditions. The predictions of each model with the numerical coalescence strains are presented in Figs. 4.28 and 4.29, respectively.

Each coalescence model gives excellent agreement with the numerical coalescence strain to a surprising level of accuracy. This is not entirely unexpected since

Table 4.4 Parameters for the void aspect ratio for an initial porosity of 1 % and a hardening exponent of 0.10

Aspect ratio	T	a_2	a_1	W_0	Limit strain ε_1	R^2	Aspect ratio at strain limit W_l	Slope for extrapolation b_l
1/6	1/3	1.21	1.27	0.17	1.200	1.000	3.430	12.000
	2/3	−0.11	1.66	0.177	0.400	1.000	0.811	1.566
	1	−1.54	1.84	0.17	0.230	1.000	0.509	1.133
	2	−4.78	2.15	0.17	0.090	1.000	0.322	1.294
	3	−13.74	2.87	0.17	0.054	1.000	0.281	1.396
1	1/3	3.05	2.36	1.00	0.800	0.999	4.838	9.000
	2/3	0.64	2.42	1.00	0.900	1.000	3.693	3.565
	1	−1.20	1.95	1.00	0.375	1.000	1.564	1.053
	2	2.25	−0.77	1.00	0.080	0.999	0.953	−0.411
	3	6.40	−3.51	1.00	0.040	0.998	0.870	−3.003
6	1/3	15.13	7.32	6.00	1.000	0.999	28.453	56.000
	2/3	5.33	6.14	6.00	1.200	1.000	21.038	26.000
	1	−1.15	2.92	6.00	0.600	0.997	7.340	1.543
	2	34.27	−25.85	6.00	0.085	0.999	4.050	−20.026
	3	47.34	−26.88	6.00	0.080	1.000	4.153	−19.306

The shaded values of b_1 were manually adjusted and do not correspond to the derivative of the quadratic correlation
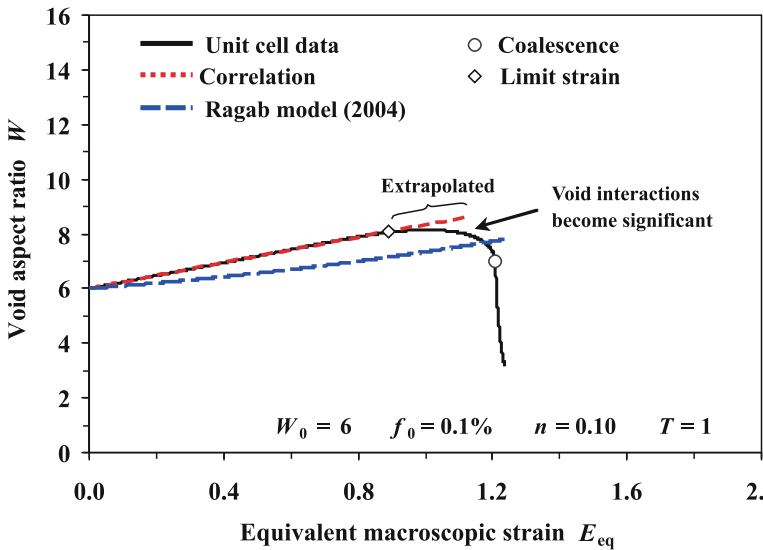

Fig. 4.26 Comparison of the void aspect correlation function with the model of Ragab (2004a) and the unit cell data. The limit strain is selected to void including the spurious interaction effects prior to coalescence
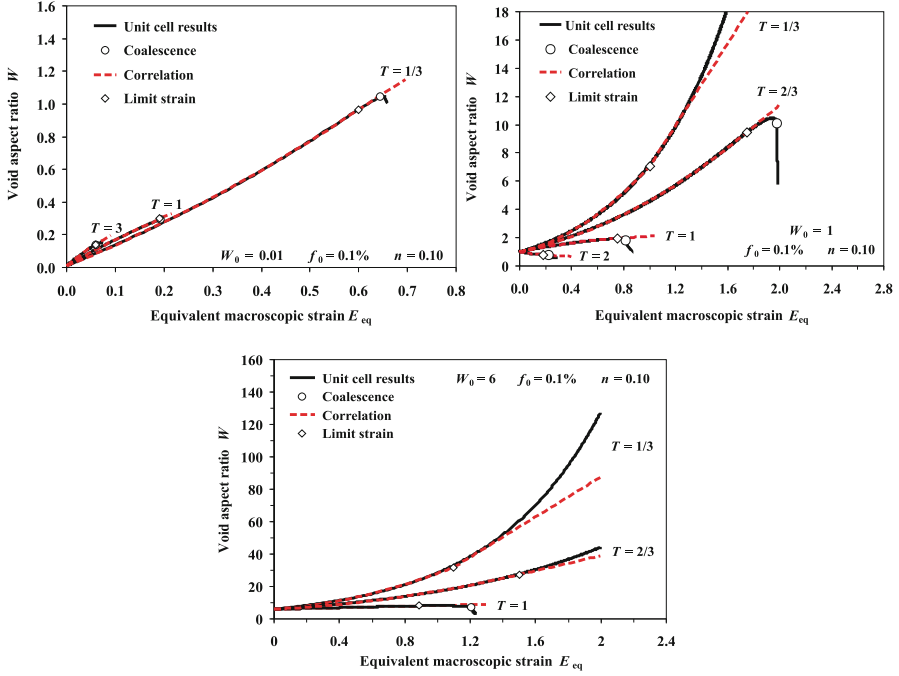
Fig. 4.27 Comparison of the void shape correlation with the unit cell data for an initially penny-shaped void (*top-left*), spherical void (*top-right*) and prolate void (*center*)
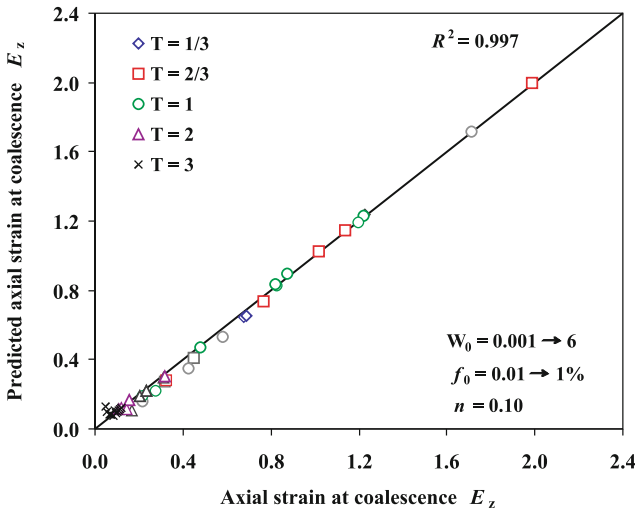

Fig. 4.28 Comparison of the numerical and predicted coalescence strains using the coalescence model of Pardoen and Hutchinson (2000) in Eq. (1.15)
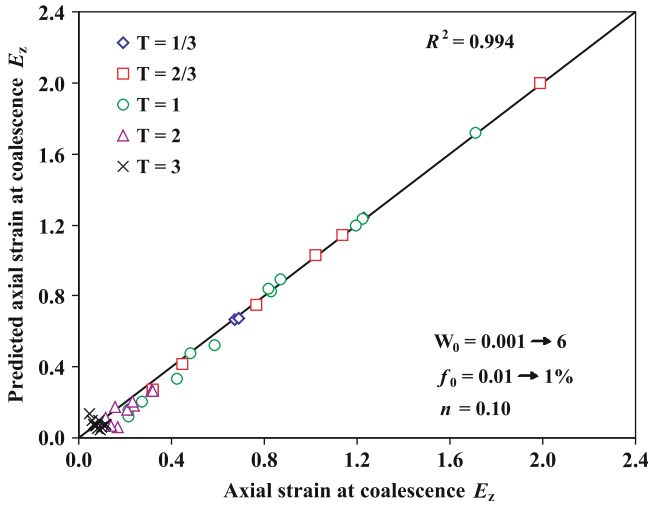
Fig. 4.29 Comparison of the numerical and predicted coalescence strains using the coalescence model of Benzerga (2002) in Eq. (1.16)

these models have been previously compared to unit cell simulations in the literature. There is no clear advantage to using either coalescence model based upon the present results. Even though the Pardoen and Hutchinson (2000) model accounts for hardening but not flat voids, and the Benzerga model (2002) assumes a perfectly plastic material, both models give very good predictions. The presence of flat voids does not translate to infinite ductilities in practice since these voids rapidly deform to shapes that are within the domain of the model. The strong agreement of both models attests to the strong underpinnings of the Thomason (1990) model that they are based upon.

The important conclusion from this validation is that the coalescence models can accurately describe void coalescence by internal necking. If the other analytical models can predict void growth and shape evolution to a similar degree of accuracy, the coalescence predictions will be sound and will agree with that of the unit cell.

4.7 Summary

A rigorous validation and calibration programme was undertaken to evaluate the analytical models used to describe void evolution and coalescence. Finite-element simulations of voided unit cells were performed to obtain benchmarks for the analytical models for a wide range of stress states. Emphasis was placed upon penny-shaped voids because they will be used extensively in the percolation model in Chap. 10 and the present evolution rules in the literature do not apply to voids of this shape. The principal contributions of this chapter are:

- The analytical models for void evolution were calibrated using the unit cell data by developing a vast library of correlation parameters.
- The semi-empirical void growth model of Ragab (2004a) was improved by calibrating the model using first-hand unit cell data and extended to the penny-shaped void regime.
- The growth and shape evolution of isolated voids within the percolation model will be representative of the actual case by virtue of the calibrated models.
- Void coalescence can be accurately predicted using the plastic limit-load model of Pardon and Hutchinson (2000) or Benzerga (2002).
- The GT yield criterion was improved by calibrating the q_2 parameter in the void growth model. Although designed for spherical voids, this calibration enables the model to give good results from penny-shaped to prolate voids